INORGANIC CHEMISTRY

Radially oriented mesoporous TiO$_2$ microspheres with single-crystal–like anatase walls for high-efficiency optoelectronic devices

Yong Liu,[1] Renchao Che,[1] Gang Chen,[2] Jianwei Fan,[1,3] Zhenkun Sun,[1] Zhangxiong Wu,[1] Minghong Wang,[1] Bin Li,[1] Jing Wei,[1] Yong Wei,[1] Geng Wang,[2] Guozhen Guan,[1] Ahmed A. Elzatahry,[4,5] Abdulaziz A. Bagabas,[6] Abdullah M. Al-Enizi,[7] Yonghui Deng,[1] Huisheng Peng,[8] Dongyuan Zhao[1]*

Highly crystalline mesoporous materials with oriented configurations are in demand for high-performance energy conversion devices. We report a simple evaporation-driven oriented assembly method to synthesize three-dimensional open mesoporous TiO$_2$ microspheres with a diameter of ~800 nm, well-controlled radially oriented hexagonal mesochannels, and crystalline anatase walls. The mesoporous TiO$_2$ spheres have a large accessible surface area (112 m^2/g), a large pore volume (0.164 cm^3/g), and highly single-crystal–like anatase walls with dominant (101) exposed facets, making them ideal for conducting mesoscopic photoanode films. Dye-sensitized solar cells (DSSCs) based on the mesoporous TiO$_2$ microspheres and commercial dye N719 have a photoelectric conversion efficiency of up to 12.1%. This evaporation-driven approach can create opportunities for tailoring the orientation of inorganic building blocks in the assembly of various mesoporous materials.

INTRODUCTION

Mesoporous semiconductors have attracted widespread interest because of their structural versatility for energy and environmental applications (1–9). Unfortunately, most of the mesoporous semiconductors have amorphous or polycrystalline pore walls that are irregularly oriented in space, adversely affecting the transport of electrons, ions, and guest molecular species in optoelectronic devices and lithium-ion batteries (10–13). This limitation could be overcome if both the orientation of mesopore channels and the nanocrystal building blocks of the channels were precisely controlled in a three-dimensional (3D) open configuration with respect to the particle surface (14–20). Although such a 3D oriented mesostructure configuration is easy to image, the actual synthesis is extremely difficult. This is because the random assembly of the surfactant micelles and inorganic oligomers spontaneously occurs as a result of the minimization of the surface energy during the assembly process (21, 22). Here, we demonstrate a simple evaporation-driven oriented assembly approach to synthesize 3D open radially oriented mesoporous TiO$_2$ microspheres with single-crystal–like anatase pore walls that dominate (101) exposed facets in an amphiphilic triblock copolymer–containing sol-gel solution. The process starts with liquid-liquid phase separation caused by the preferential evaporation of tetrahydrofuran (THF) solvent at a low temperature of 40°C; uniform 3D mesoporous TiO$_2$ microspheres assembled by PEO-PPO-PEO [poly(ethylene oxide)–poly(propylene oxide)–poly(ethylene oxide)]/titania oligomer spherical composite micelles form at the liquid-liquid phase interface. Continuous evaporation of the residual THF and hydrolyzed solvents at 80°C drives the oriented growth of both mesochannels and nanocrystal building blocks from the initially formed spherical composite micelles along the free radial and restricted tangential direction within the TiO$_2$ microspheres. This yields 3D open, radially-oriented mesoporous TiO$_2$ microspheres with single-crystalline–like anatase walls that dominate (101) exposed facets (Fig. 1 and figs. S1 to S5). The unique mesoporous TiO$_2$ microspheres can be used for dye-sensitized solar cells (DSSCs) with commercial dye N719, revealing an excellent photoelectric conversion efficiency.

RESULTS

In situ synchrotron radiation small-angle x-ray scattering (SAXS) patterns of the products harvested at different intervals of time from the preparation (Fig. 2, A to E) confirm the transformation of the initial PEO-PPO-PEO/titania oligomers from spherical micelles (cubic $Im\overline{3}m$ mesophase) to radial cylindrical micelles (hexagonal $p6mm$ mesophase). After evaporation at 40°C for 6 hours, distinct diffraction arcs are observed, as shown in the 2D SAXS image (Fig. 2B), which can be indexed to a cubic mesophase (space group $Im\overline{3}m$), indicating that the spherical composite micelles were initially oriented 2D in the membrane form at the interface between the THF- and water-rich phases. Transmission electron microscopy (TEM) images (figs. S2 and S3) show that with continuous solvent evaporation at 40°C for 20 hours, the spherical composite micelles further aggregate together to form large, dense 3D spherical particles with improved cubic $Im\overline{3}m$ symmetry, consistent with the appearance of high-order reflections for (220), (310), and (330)

[1]Department of Chemistry, Shanghai Key Laboratory of Molecular Catalysis and Innovative Materials, Key Laboratory of Molecular Engineering of Polymers, iChEM (Collaborative Innovation Center of Chemistry for Energy Materials), Laboratory of Advanced Materials, Fudan University, Shanghai 200433, China. [2]Shanghai Synchrotron Radiation Facility, Shanghai Institute of Applied Physics, Chinese Academy of Sciences, Shanghai 201204, China. [3]College of Environmental Science and Engineering, State Key Laboratory of Pollution Control and Resource Reuse, Tongji University, Shanghai 200092, China. [4]Materials Science and Technology Program, College of Arts and Sciences, Qatar University, P. O. Box 2713, Doha, Qatar. [5]Polymer Materials Research Department, Advanced Technology and New Materials Research Institute, City of Scientific Research and Technology Applications, New Borg El-Arab City, Alexandria 21934, Egypt. [6]National Petrochemical Technology Center (NPTC), Materials Science Research Institute (MSRI), King Abdulaziz City for Science and Technology (KACST), P. O. Box 6086, Riyadh 11442, Kingdom of Saudi Arabia. [7]Department of Chemistry, College of Science, King Saud University, Riyadh 11451, Kingdom of Saudi Arabia. [8]State Key Laboratory of Molecular Engineering of Polymers, Department of Macromolecular Science, and Laboratory of Advanced Materials, Fudan University, Shanghai 200438, China.
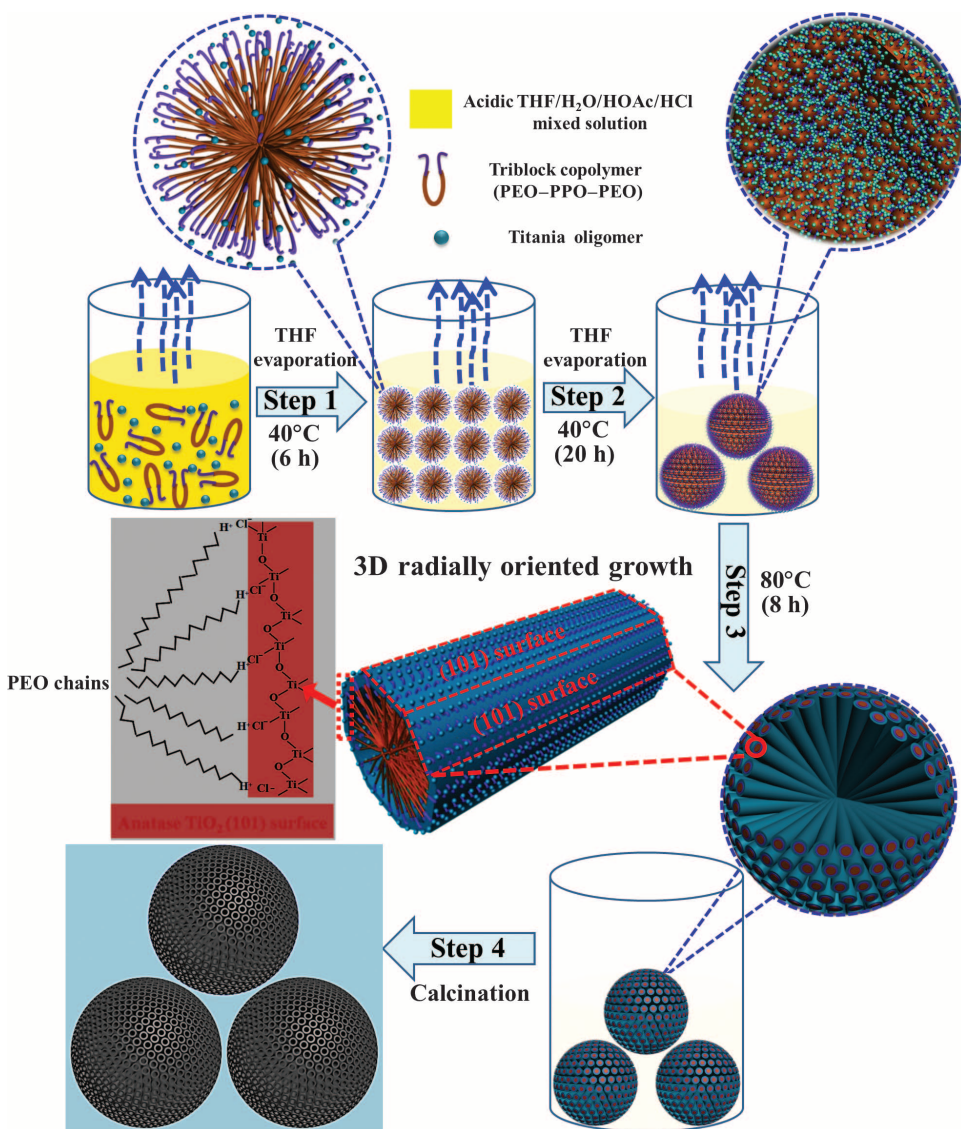*Corresponding author. E-mail: dyzhao@fudan.edu.cn

Liu et al. Sci. Adv. 2015;1:e1500166   8 May 2015

1 of 8

Fig. 1. Schematic representation of the formation process through evaporation-driven oriented assembly. Step 1: Formation of the PEO-PPO-PEO/titania oligomer composite spherical micelles with PPO segments as a core and titania-associated PEO segments as a shell with the initial preferential evaporation of THF solvent at 40°C for 6 hours. **Step 2**: Aggregation of the composite spherical micelles into big spheres on the interface of the poor solvent water-rich phase, which is driven by the increasing concentration of the spherical micelles and the requirement of minimization of interface energy. **Step 3**: The second-step evaporation of THF and residual solvents hydrolyzed from titanium tetrabutoxide (TBOT) precursor (further treated at 80°C for 8 hours) could further drive the composite spherical micelles to fuse into cylinders, leading to continuous 3D radially-oriented growth of cylindrical micelles and TiO₂ nanoentities. **Step 4**: The 3D open radially oriented mesoporous TiO₂ microspheres with single-crystal–like anatase walls that dominate (101) facets are obtained by removing the triblock copolymer templates after calcination in air at 400°C for 2 hours.

planes (Fig. 2, A and C). After the final-step evaporation of solvents at 80°C for 8 hours, the SAXS pattern of the as-made PEO-PPO-PEO/titania composite microspheres (Fig. 2, A and D) shows two intense scattering peaks with lattice spacing $d_{100} = 13.47$ nm and $d_{110} = 7.76$ nm ($d_{100}/d_{110} =$ 1: $\sqrt{3}$). The second-order reflection confirmed both the periodicity and the orientation of the 3D radially aligned hexagonal cylindrical

pores, suggesting structural transformation from a cubic to a hexagonal mesostructure. The wide-angle x-ray diffraction (WAXRD) patterns show that evaporation treatment at 80°C can lead to crystallization and oriented growth of anatase walls (fig. S4). After removal of the amphiphilic triblock copolymer templates by calcination at 400°C for 2 hours, the obtained mesoporous TiO₂ microspheres exhibited similar SAXS peaks at higher q values with $d_{100} = 12.12$ nm and $d_{110} =$ 6.98 nm (Fig. 2, A and E), indicating that the 3D hexagonal cylindrical mesostructure was retained.

Scanning electron microscopy (SEM) and TEM images (Fig. 2, F to I) show that the products consist of uniform spheres with a diameter of ~800 nm after calcination. The cylindrical open pores exposed on the rough surface of the microspheres can be observed in the inset of Fig. 2F. The center-to-center distance between two adjacent cylindrical mesopore channels was on average ~11.8 nm, and the pore size was estimated to be ~5.5 nm. Close inspection of the mesoporous TiO₂ microspheres (Fig. 2G) revealed that the close-packed cylindrical mesochannels were arranged radially from the center to the surface. A large number of interchannel pores with diameters of ~5 to 15 nm were observed on the wall surface of cylindrical mesopore channels (marked by red circles in Fig. 2G). Such a pore arrangement model can be further discerned from high-angle annular dark-field scanning TEM (HAADF-STEM) images of a single microsphere (fig. S6). The cylindrical pore size can be enlarged to 5 to 10 nm when the final evaporation temperature increases from 80° to 120°C (fig. S7). To confirm the internal structure, we examined the ultramicrotomed sections of a single mesoporous TiO₂ microsphere using TEM technique. The results revealed that the cylindrical mesopores were distributed radially from the center to the surface along the radial and restricted tangential direction, and all the mesopores were regularly arranged and highly open (Fig. 2, H and I, and fig. S8). Considering a spherically symmetric model of the mesoporous TiO₂ microspheres, some of the cylindrical pores deviated slightly from the hexagonal symmetry and branched into two hexagonal channels in between (23).

High-resolution TEM (HRTEM) images and selected-area electron diffraction (SAED) patterns further reveal that the radially arranged mesopore walls have a single-crystal–like anatase characteristic (Fig. 3
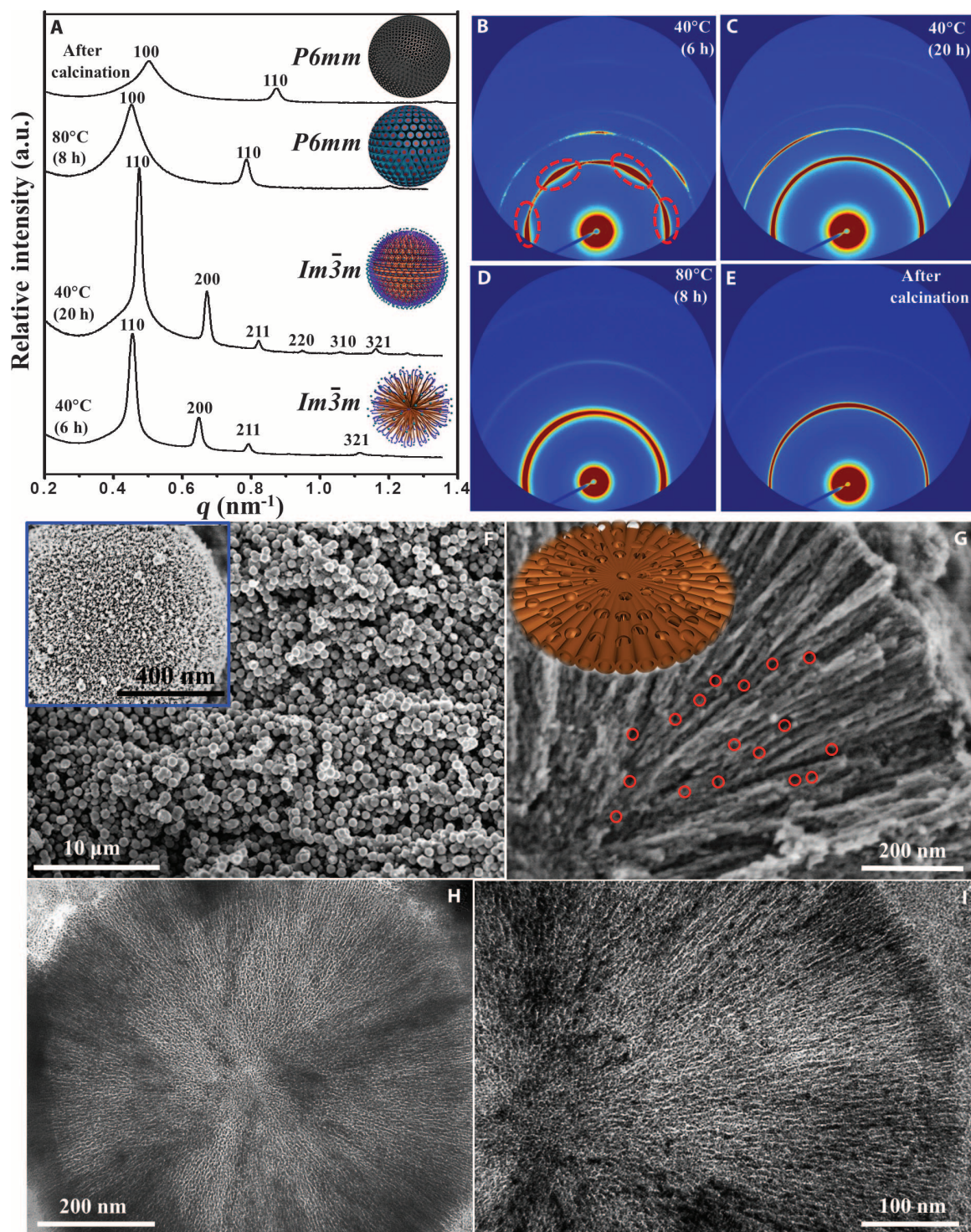
Fig. 2. Microstructure characterization of the radially oriented mesoporous TiO₂ microspheres. (A) In situ synchrotron radiation 1D SAXS patterns of the mesoporous TiO$_2$ microsphere products harvested at different intervals of reaction time. Insets: Corresponding schematic representation of the four samples. a.u., arbitrary units. (B to E) 2D SAXS images of the four samples. (F) SEM image of the mesoporous TiO$_2$ microspheres. Inset: SEM image of a single mesoporous TiO$_2$ microsphere. (G) SEM image of a single ultramicrotomed, radially-oriented mesoporous TiO$_2$ microsphere with a large number of interchannel pores (~5 to 15 nm in diameter, marked by red circles). Inset: Corresponding schematic representation of the structure models for the radially oriented channels with interchannel pores. (H and I) TEM images of a single ultramicrotomed, mesoporous TiO$_2$ microsphere.
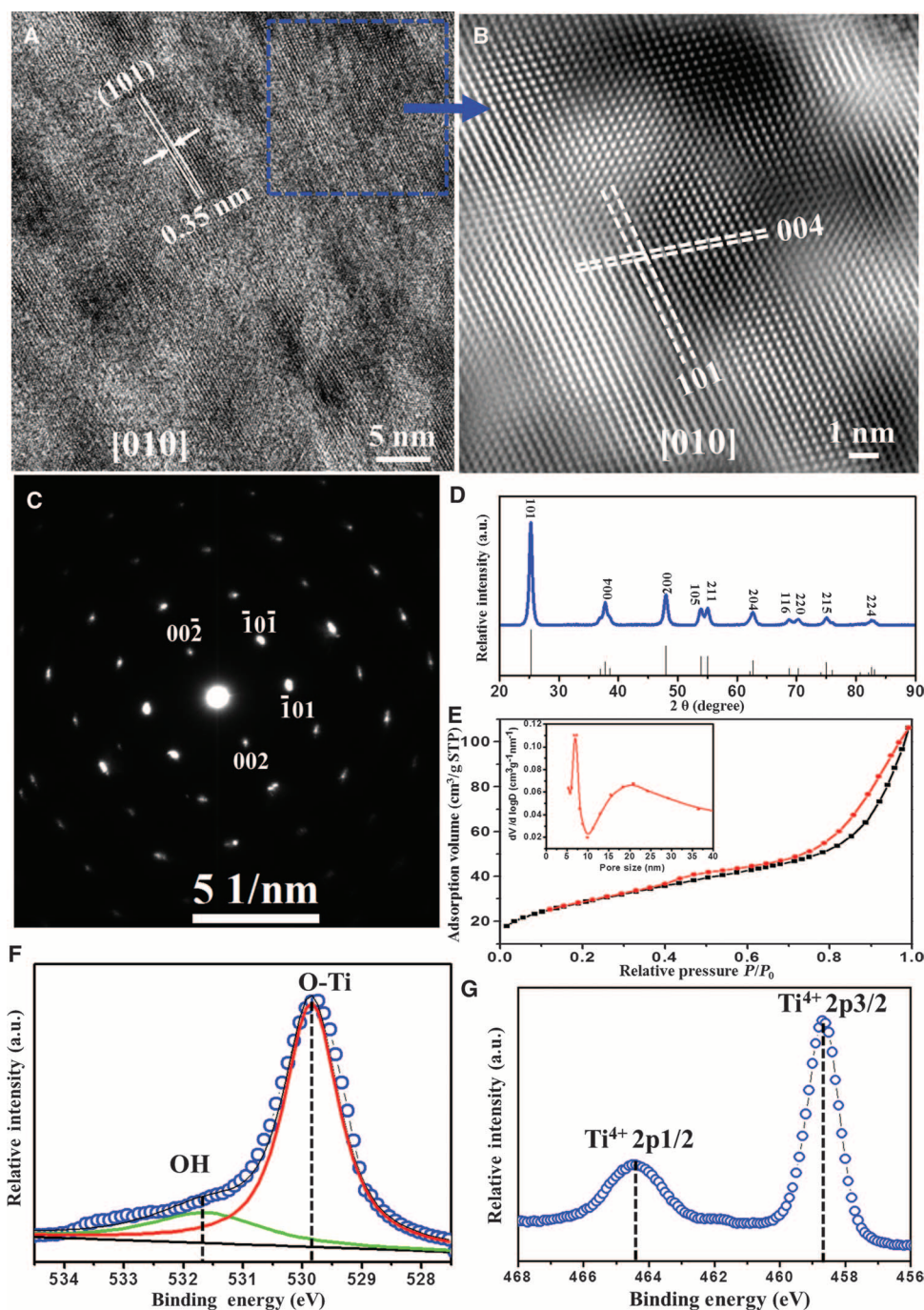
Fig. 3. Single-crystal pore wall characterizations. (**A**) HRTEM images taken from the area of the cylindrical mesopore bundles of an ultramicrotomed, mesoporous TiO₂ microsphere with [010] incidence, perpendicular to the mesopore channels. (**B**) A fast Fourier transform–filtered TEM image recorded from the dotted square area in (A). (**C**) The SAED pattern taken from the cylindrical pore bundles region with [010] incidence. (**D**) The WAXRD pattern of the mesoporous TiO₂ microspheres, compared to the standard anatase (space group $I4_1/amd$, JCPDS card no. 21-1272). (**E**) Nitrogen adsorption-desorption isotherms; inset: pore size distributions of the mesoporous TiO₂ microspheres with two sets of pores. The primary pore size is centered at 5.7 nm, and the secondary pore size at 10 to 30 nm. (**F** and **G**) XPS core-level spectra of Ti2p and O1s, respectively, for the mesoporous TiO₂ microspheres.

and figs. S9 and S10). The lattice fringe distance perpendicular to the pore walls is ~0.238 nm, which corresponds to the interplanar distance of the (004) atomic plane in anatase, indicating that the mesopore walls grow with a preferred [001] orientation (Fig. 3, A and B, and fig. S10A). The interfacial angle between two adjacent faces is ~68.3° (Fig. 3B and fig. S10C), which is the same as the theoretical value for the angle between the (004) and (101) planes of anatase (24), suggesting that the (101) plane is the dominant exposed facet along the pore walls. A fast Fourier transform–filtered TEM image (fig. S10D) and SAED patterns (Fig. 3C and fig. S9, A to D) show slightly elongated diffraction spots and a slightly distorted hexagonal symmetry. Such distorted cylindrical pore channels can cause some lattice distortion between the boundaries of the crystalline domains when they are assembled in a radial and restricted tangential direction to form single-crystal–like TiO₂ pore frameworks (18, 25). The WAXRD pattern (Fig. 3D) confirms the highly crystalline anatase phase (space group $I4_1/amd$) of the radially oriented mesoporous TiO₂ microspheres. Nitrogen adsorption-desorption isotherms showed characteristic type IV curves with two distinguishable capillary condensation steps (Fig. 3E). A distinct capillary condensation step at P/P_0 = 0.40 to 0.7 reflected uniform cylindrical mesopores resulting from the radial primary mesopore channels of the TiO₂ microspheres. Moreover, a hysteresis loop at a higher pressure (P/P_0 = 0.90 to 0.99) reflected the interchannel mesopores from the structural defects, consistent with the results from the HRTEM and HAADF-STEM images. The pore size distribution calculated using the Barrett-Joyner-Halenda (BJH) model (inset of Fig. 3E) showed two sets of pores. The primary pore size is centered at 5.7 nm, and the secondary pore size is 10 to 30 nm, which agrees well with that estimated from the SEM and TEM images. The Brunner-Emmet-Teller (BET) surface area and pore volume were calculated to be as high as 112 m²/g and 0.164 cm³/g, respectively. The x-ray photoelectron spectroscopy (XPS) results for the mesoporous TiO₂ microspheres indicate the Ti⁴⁺ oxidation state (Fig. 3F) and the presence of lattice oxygen, O-Ti⁴⁺ and Ti-OH (Fig. 3G). The O-Ti⁴⁺ and massive Ti-OH groups on the surface can act as binding dye and work as charge transfer channels (26).

The loading capacity of the commercial dye N719 in the mesoporous TiO_2 microspheres was ~2.13×10^{-7} mol cm^{-2}, about twice those of the frequently used commercial Degussa TiO_2 P25 (1.12×10^{-7} mol cm^{-2}) and conventional mesoporous TiO_2 bulk (1.45×10^{-7} mol cm^{-2}). Such high dye loading could be attributed to the large accessible surface area and the single-crystal–like anatase walls with dominant (101) exposed facets. The anatase (101) facet here is believed to be the best surface for loading N719 dye because the distance between two binding carboxylate groups of N719 dye matches well with the distance between Ti atoms on anatase (101) facets (20). In addition, the electrode films based on the mesoporous TiO_2 microspheres have high light-scattering capacity in the visible and near-infrared (NIR) regions (400 to 800 nm) (Fig. 4A), indicating that the incident sunlight can be significantly scattered within the film.

To investigate the photovoltaic performance of DSSCs, we compared their current density (J)–voltage (V) characteristics with those of conventional mesoporous TiO_2 bulk with randomly oriented pore channels and P25 under simulated AM 1.5 light (Fig. 4B). The DSSCs based on radially oriented mesoporous TiO_2 microspheres showed an ultrahigh short-circuit photocurrent density (J_{sc}) of ~22.91 mA cm^{-2}, an open-circuit voltage (V_{oc}) of ~0.75 V, and a fill factor of ~0.71, yielding a power conversion efficiency (PCE) of ~12.1%. The DSSC performance measurements were repeated several times for 15 individual solar cells, and the obtained PCE had a close average value of ~12.1% (fig. S11), which was also confirmed by an accredited photovoltaic calibration laboratory (fig. S12), indicating a good reliability of the DSSCs. In contrast, the PCEs are ~7.6 and 6.8% for the DSSCs based on the conventional mesoporous TiO_2 and P25, respectively (Table 1 and Fig. 4B).

Figure 4C and fig. S13 show the cross-sectional SEM image of a typical mesoporous TiO_2 microsphere–based film device. All the mesoporous TiO_2 electrodes were sensitized with commercially available N719 dye, and the film thickness was ~14 μm. The incident photo–to–current conversion efficiency (IPCE) of the mesoporous TiO_2 microspheres exceeded 60% in a broad spectral range from 300 to 700 nm, reaching its maximum of ~95% at 530 nm (Fig. 4D). The photoresponse region was remarkably extended over 800 nm for the DSSCs based on the radially oriented single-crystal–like mesoporous TiO_2 microspheres. Such an expanded photo-responsive behavior is at-
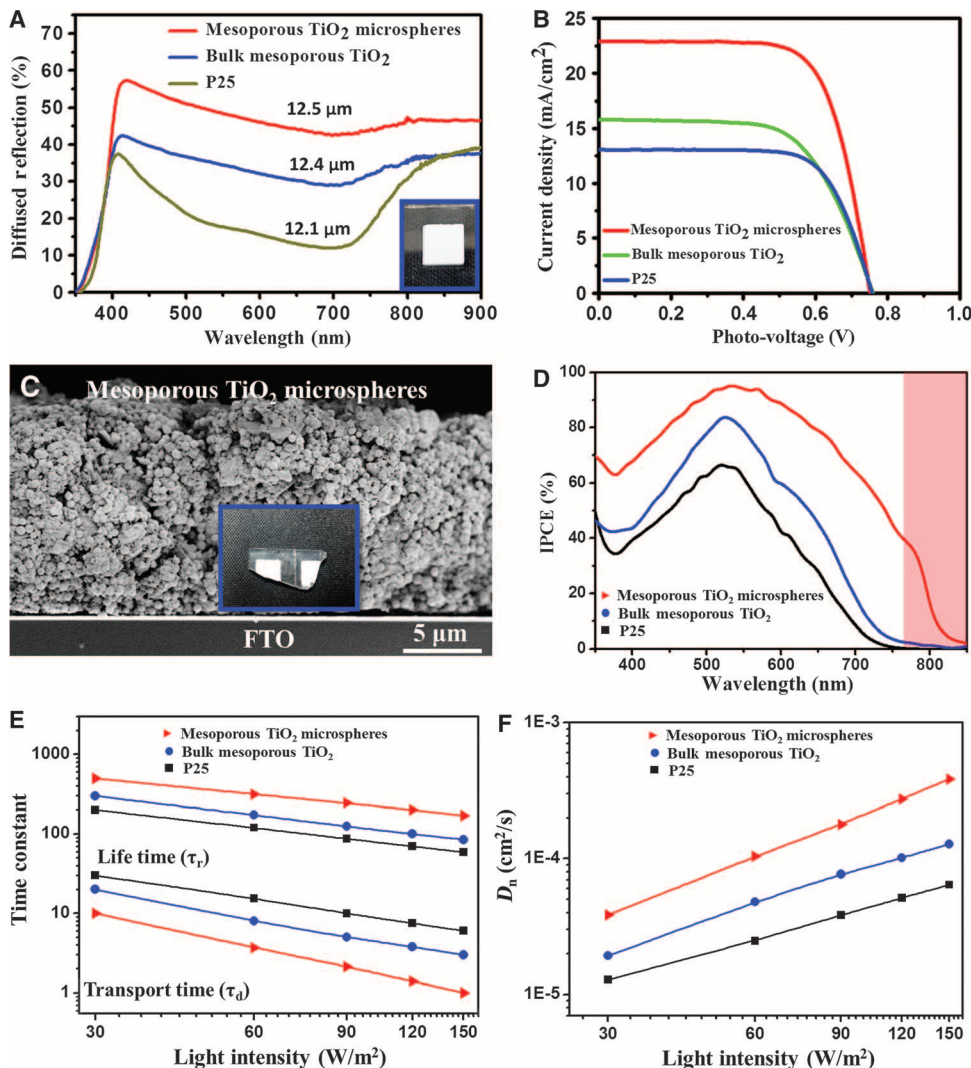
Fig. 4. Photovoltaic device characterization. (A) Diffuse reflectance spectra of TiO_2 films with a thickness of about 12 μm. Inset: Photograph of the 3D open, radially-oriented mesoporous TiO_2 microsphere-based film. **(B)** J-V curves of DSSCs fabricated from the three TiO_2 samples with N719 dye under AM 1.5G simulated sunlight with a power density of 100 mW cm^{-2}. **(C)** A cross-sectional SEM image of a DSSC composed of 3D open mesoporous TiO_2 microspheres. Inset: Photograph of the sliced films for SEM. **(D)** IPCE spectra of the DSSCs based on the radially oriented mesoporous TiO_2 spheres with a uniform size of 800 nm, conventional mesoporous TiO_2 bulk, and commercial Degussa TiO_2 P25. The pink marked shadow region shows that the photo-response region is extended over 800 nm for the single-crystal–like mesoporous TiO_2 microspheres. **(E)** Electron transport time and electron lifetime. **(F)** Electron diffusion coefficient (D_n) for the mesoporous TiO_2 microspheres.

tributed to the 3D open, radially-oriented mesopore configuration and large particle size (~800 nm) of the mesoporous TiO_2 microspheres, which results in the pronounced light-scattering property and expanded photo-responsive ability in the NIR region. From the overlap integral with the standard global AM 1.5 solar emission spectrum, the integrated photocurrent density from the IPCE spectrum was calculated as 19.7 mA cm^{-2}, which is 86% of the measured J_{sc} value (22.9 mA cm^{-2}). The experimental J_{sc} error between the J-V curve and IPCE was ~14%. This is probably due to the spectral mismatch between the two simulated solar lights in the two separated instruments.

Table 1. Photovoltaic parameters of DSSCs based on the photoanodes of radially oriented mesoporous TiO_2 microspheres, bulk mesoporous TiO_2, and commercial P25 after $TiCl_4$ treatment [measured under AM 1.5 sunlight illumination (100 mW cm^{-2})]. The active area of the devices with a metal mask was about 0.16 cm^2. FF, fill factor.

Samples	V_{oc} (mV)	J_{sc} (mA cm^{-2})	FF (%)	η (%)	Adsorbed dye (×10^{-7} mol cm^{-2})*
Mesoporous TiO_2 microspheres	751	22.9	70.6	12.1	2.13
Bulk mesoporous TiO_2	759	15.8	63.1	7.6	1.45
P25	734	12.3	75.0	6.8	1.12

*Dye-adsorbed films with an area of ~10 cm^2 were used for estimating the adsorbed dye concentration. The commercial N719 dye was first desorbed into a 0.1 M NaOH solution in water and ethanol [1:1 (v/v)], and the desorbed N719 dye concentration was then measured by using an ultraviolet-visible spectrophotometer.

The transport time (τ_d), electron lifetime (τ_r), and diffusion coefficient (D_n), calculated using intensity-modulated photocurrent spectroscopy (IMPS) and intensity-modulated photovoltage spectroscopy (IMVS) (Fig. 4, E and F), demonstrate that the electron transportation rate within the mesoporous TiO_2 microspheres is more rapid than those inside the mesoporous TiO_2 bulk and P25, and the charge recombination is relatively more suppressed at the mesoporous TiO_2 microsphere photoanode-electrolyte interface (27, 28).

On the basis of the above characterization of the DSSCs, the high PCE of the mesoporous TiO_2 microspheres was associated with the high loading capacity of N719 dye and the large accessible surface area with dominant (101) exposed facets, high rate of electron transfer through single-crystalline–like anatase walls, and pronounced light-scattering ability due to 3D open, radially-oriented mesopore configuration. The mesoporous TiO_2 microspheres also demonstrated high performance in photocatalytic reactions (fig. S14).

To understand the evaporation-driven oriented assembly process, we used the cryo-SEM technique to examine the products harvested from the sol solution at different intervals of time (fig. S15). The growth of these mesoporous TiO_2 microspheres was found to proceed through a phase separation and gradual transformation of Pluronic/titania composites from spherical to radial cylindrical micelles. At the first stage of the process, the preferential evaporation of THF at 40°C increased the concentration of the mixed solution (containing water, HCl, acetic acid, amphiphilic block copolymer, and titania oligomers), inducing a liquid-liquid phase separation by hydrolytic polycondensation of the TBOT precursor. The spherical PEO-PPO-PEO/titania composite micelles formed at the interface between the THF- and water-rich phases, minimizing the surface tension (fig. S15B). TEM images show that these spherical micelles have a typical core-shell structure with PEO-PPO-PEO as the core and titania oligomers as the shell (fig. S2). With continuous THF evaporation at 40°C, these small spherical micelles aggregated together to form large, dense, spherical particles, reducing interface energy; hence, the solution became turbid (fig. S15C). Finally, second-step evaporation of THF and residual solvents (such as butyl alcohol) from inside the microspheres (at 80°C) caused the PEO-PPO-PEO/titania spherical micelles to fuse into cylinders, leading to a continuous 3D radially oriented growth of cylindrical micelles (fig. S15D). This driving force was the result of reducing surface energy when the interface between the spherical composite micelles and THF solvent disappeared after complete solvent evaporation.

DISCUSSION

The oriented growth of the single-crystal–like anatase pore walls along the [001] direction is related to the solvent evaporation–driven oriented assembly growth process (24, 29, 30). The addition of a strong aqueous acid (HCl) can partially charge the initially formed anatase nanocrystals by selective adsorption of Cl$^-$ ions on the (101) planes (Fig. 1 and fig. S5) (24), which may act as a "bridge" between the nanocrystal building blocks and hydrophilic segment boundary of Pluronic F127. The STEM image and energy-dispersive x-ray spectroscopy (EDX) element mapping analyses confirm the presence of Cl$^-$ ions on the crystallographic planes of a single ultramicrotomed TiO_2 microsphere (fig. S16). As confirmed by in situ synchrotron radiation SAXS (Fig. 2A), a continuous slow evaporation of the residual THF and hydrolyzed solvent (for example, n-butyl alcohol) at 80°C actually causes the initially formed spherical micelles to fuse into radially oriented cylindrical micelles. Simultaneously, this second-step evaporation from the center to the outside of the sphere particles can also cause TiO_2 crystallization oriented around F127 cylindrical micelles at a low temperature of 80°C. Our results revealed that the slow evaporation and confinement of the triblock copolymer hydrophilic boundary could correct the crystallographic orientation of the nanocrystal building blocks. After calcination at 400°C for 2 hours, the oriented anatase nanocrystals can further crystallize into single-crystal–like pore walls with dominant (101) exposed facets. However, the products obtained in the same conditions without F127 are typically crackable monoliths composed of aggregates of irregular TiO_2 nanocrystals (fig. S17), indicating that Pluronic F127 is an essential template in the evaporation-driven oriented growth of mesoporous TiO_2 microspheres.

Furthermore, conventional mesoporous TiO_2 bulk with irregularly oriented cylindrical pores and polycrystalline walls can be obtained (figs. S18 and S19) when the initial yellow sol-gel reaction solution (fig. S1A) evaporates quickly under a low-vacuum condition (~200 Pa) at 40°C, implying that control of the solvent evaporation rate is vital for the micelles and inorganic nanoentities to adapt their preferred orientation to the interface. Thus, if proper control of the solvent evaporation rate and initial soluble precursors is achieved, this general evaporation-driven oriented assembly method can easily extend the synthesis of mesoporous oriented single crystals to a range of functional semiconductors.

In summary, well-defined, uniform 3D open, mesoporous TiO_2 microspheres with radially oriented mesochannels and single-crystal–like pore walls that dominate (101) exposed facets have been successfully synthesized by a novel evaporation-driven oriented assembly method. Such an unprecedented type of 3D open, mesoporous TiO_2 microsphere has a large accessible surface area (112 m^2/g), a large pore volume (0.164 cm^3/g), highly single-crystalline–like walls, and a uniform submicrometer size. Owing to their unique features, especially dominant (101) exposed facets and large surface area, the resultant DSSCs have a high energy-conversion efficiency of up to 12.1%. Such a general evaporation-driven oriented assembly procedure results in a dramatic transformation of surfactant/inorganic oligomer micelles from spherically to radially oriented cylindrical micelles by controlling the solvent step evaporation. This evaporation-driven oriented assembly method

can be easily extended to synthesize highly crystalline mesoporous materials with oriented configuration for advanced applications in sensors, photocatalysis, drug delivery, etc.

MATERIALS AND METHODS

The 3D open, radially-oriented TiO_2 microspheres were synthesized by the evaporation-driven oriented assembly (EDOA) approach (see Supplementary Materials and Methods for detailed preparation of TiO_2 microspheres). In summary, Pluronic F127 ($PEO_{106}PPO_{70}PEO_{106}$, weight-average molecular weight = 12,600 g/mol), water, acetic acid, concentrated HCl (36 wt %), and TBOT were vigorously stirred in THF solvent to form a clear, golden yellow solution. Sequentially, the obtained clear solution was transferred into a volumetric flask and left in a drying oven to evaporate the THF solvent at 40°C for 8 hours, then at 80°C for another 12 hours to completely remove the solvent. Finally, the white TiO_2 mesoporous powder was obtained by calcination in air at 450°C for 3 hours. The detailed methods and characterization are available in the Supplementary Materials.

SUPPLEMENTARY MATERIALS

Supplementary material for this article is available at http://advances.sciencemag.org/cgi/content/full/1/4/e1500166/DC1

Materials and Methods

Fig. S1. Photographs of the mixed solution for the preparation of the mesoporous TiO_2 microspheres during the evaporation of the solvent THF.

Fig. S2. TEM images with different magnifications of the sample taken from the preparation solution after the solvent evaporation at 40°C for 6 hours.

Fig. S3. STEM image and EDX elemental maps of the sample taken from the preparation solution after THF evaporation at 40°C for 6 hours.

Fig. S4. WAXRD patterns of the precipitates obtained at different solvent evaporation times without calcination.

Fig. S5. The proposed mechanism for oriented growth of the anatase single-crystal–like pore walls.

Fig. S6. HAADF-STEM images of a single ultramicrotomed 3D open radially oriented mesoporous TiO_2 microsphere.

Fig. S7. SEM images of the products obtained after the second-step evaporation at a high temperature of 120°C.

Fig. S8. TEM images of an ultramicrotomed radially oriented mesoporous TiO_2 microsphere with different integrity.

Fig. S9. SAED and HRTEM images taken from the cylindrical pore bundle regions with different orientation.

Fig. S10. HRTEM and SEAD images of the mesoporous TiO_2 spheres taken from the area of the cylindrical pore bundles.

Fig. S11. Detail photovoltaic parameters of 15 individual mesoporous TiO_2 microsphere-based cells.

Fig. S12. Independent certificate by the National Center of Supervision and Inspection on Solar Photovoltaic Products Quality.

Fig. S13. Cross-sectional and top-view SEM images of the photoanode film based on the uniform mesoporous TiO_2 microspheres.

Fig. S14. Photocatalytic decomposition of methylene blue dye over the mesoporous TiO_2 microspheres.

Fig. S15. Cryo-SEM images of the samples harvested at different intervals of solvent evaporation time.

Fig. S16. STEM image and EDX elemental maps of a single ultramicrotomed mesoporous TiO_2 microsphere.

Fig. S17. SEM images of the products obtained under similar conditions in the absence of Pluronic F127.

Fig. S18. Field-emission SEM (FESEM) and TEM images of the ordered mesoporous TiO_2 bulks with randomly oriented cylindrical pores.

Fig. S19. HRTEM images, nitrogen adsorption-desorption isotherms, pore size distributions, and SAXS integral curves of the randomly oriented mesoporous TiO_2 bulk samples.

REFERENCES AND NOTES

1. D. Zhao, J. Feng, Q. Huo, N. Melosh, G. H. Fredrickson, B. F. Chmelka, G. D. Stucky, Triblock copolymer syntheses of mesoporous silica with periodic 50 to 300 angstrom pores. *Science* **279**, 548–552 (1998).

2. U. Bach, D. Lupo, P. Comte, J. Moser, F. Weissörtel, J. Salbeck, H. Spreitzer, M. Grätzel, Solid-state dye-sensitized mesoporous TiO_2 solar cells with high photon-to-electron conversion efficiencies. *Nature* **395**, 583–585 (1998).

3. T. Suteewong, H. Sai, R. Hovden, D. Muller, M. S. Bradbury, S. M. Gruner, U. Wiesner, Multi-compartment mesoporous silica nanoparticles with branched shapes: An epitaxial growth mechanism. *Science* **340**, 337–341 (2013).

4. P. Yang, D. Zhao, D. I. Margolese, B. F. Chmelka, G. D. Stucky, Generalized syntheses of large-pore mesoporous metal oxides with semicrystalline frameworks. *Nature* **396**, 152–155 (1998).

5. G. S. Armatas, M. G. Kanatzidis, Hexagonal mesoporous germanium. *Science* **313**, 817–820 (2006).

6. E. J. Crossland, N. Noel, V. Sivaram, T. Leijtens, J. A. Alexander-Webber, H. J. Snaith, Mesoporous TiO_2 single crystals delivering enhanced mobility and optoelectronic device performance. *Nature* **495**, 215–219 (2013).

7. B. Tian, X. Liu, B. Tu, C. Yu, J. Fan, L. Wang, S. Xie, G. D. Stucky, D. Zhao, Self-adjusted synthesis of ordered stable mesoporous minerals by acid–base pairs. *Nat. Mater.* **2**, 159–163 (2003).

8. F. Sauvage, D. Chen, P. Comte, F. Huang, L.-P. Heiniger, Y.-B. Cheng, R. A. Caruso, M. Graetzel, Dye-sensitized solar cells employing a single film of mesoporous TiO_2 beads achieve power conversion efficiencies over 10%. *ACS Nano* **4**, 4420–4425 (2010).

9. Z.-R. Tian, W. Tong, J.-Y. Wang, N.-G. Duan, V. V. Krishnan, S. L. Suib, Manganese oxide mesoporous structures: Mixed-valent semiconducting catalysts. *Science* **276**, 926–930 (1997).

10. D. Li, H. Zhou, I. Honma, Design and synthesis of self-ordered mesoporous nanocomposite through controlled in-situ crystallization. *Nat. Mater.* **3**, 65–72 (2003).

11. S. Inagaki, S. Guan, T. Ohsuna, O. Terasaki, An ordered mesoporous organosilica hybrid material with a crystal-like wall structure. *Nature* **416**, 304–307 (2002).

12. K. C.-W. Wu, X. Jiang, Y. Yamauchi, New trend on mesoporous films: Precise controls of one-dimensional (1D) mesochannels toward innovative applications. *J. Mater. Chem.* **21**, 8934–8939 (2011).

13. J. Lee, M. C. Orilall, S. C. Warren, M. Kamperman, F. J. DiSalvo, U. Wiesner, Direct access to thermally stable and highly crystalline mesoporous transition-metal oxides with uniform pores. *Nat. Mater.* **7**, 222–228 (2008).

14. A. Walcarius, E. Sibottier, M. Etienne, J. Ghanbaja, Electrochemically assisted self-assembly of mesoporous silica thin films. *Nat. Mater.* **6**, 602–608 (2007).

15. E. K. Richman, T. Brezesinski, S. H. Tolbert, Vertically oriented hexagonal mesoporous films formed through nanometre-scale epitaxy. *Nat. Mater.* **7**, 712–717 (2008).

16. F. Shan, X. Lu, Q. Zhang, J. Wu, Y. Wang, F. Bian, Q. Lu, Z. Fei, P. J. Dyson, A facile approach for controlling the orientation of one-dimensional mesochannels in mesoporous titania films. *J. Am. Chem. Soc.* **134**, 20238–20241 (2012).

17. C.-W. Wu, T. Ohsuna, M. Kuwabara, K. Kuroda, Formation of highly ordered mesoporous titania films consisting of crystalline nanopillars with inverse mesospace by structural transformation. *J. Am. Chem. Soc.* **128**, 4544–4545 (2006).

18. H. Cölfen, M. Antonietti, Mesocrystals: Inorganic superstructures made by highly parallel crystallization and controlled alignment. *Angew. Chem. Int. Ed. Engl.* **44**, 5576–5591 (2005).

19. B. Liu, E. S. Aydil, Growth of oriented single-crystalline rutile TiO_2 nanorods on transparent conducting substrates for dye-sensitized solar cells. *J. Am. Chem. Soc.* **131**, 3985–3990 (2009).

20. M. Adachi, Y. Murata, J. Takao, J. Jiu, M. Sakamoto, F. Wang, Highly efficient dye-sensitized solar cells with a titania thin-film electrode composed of a network structure of single-crystal-like TiO_2 nanowires made by the "oriented attachment" mechanism. *J. Am. Chem. Soc.* **126**, 14943–14949 (2004).

21. Z. Teng, G. Zheng, Y. Dou, W. Li, C. Y. Mou, X. Zhang, A. M. Asiri, D. Zhao, Highly ordered mesoporous silica films with perpendicular mesochannels by a simple Stöber-solution growth approach. *Angew. Chem. Int. Ed. Engl.* **51**, 2173–2177 (2012).

22. H. Yang, A. Kuperman, N. Coombs, S. Mamiche-Afara, G. A. Ozin, Synthesis of oriented films of mesoporous silica on mica. *Nature* **379**, 703–705 (1996).

23. B. Pauwels, G. Van Tendeloo, C. Thoelen, W. Van Rhijn, P. A. Jacobs, Antisense expression of a cell wall–associated protein kinase, WAK4, inhibits cell elongation and alters morphology. *Adv. Mater.* **13**, 1317 (2001).

24. H. G. Yang, C. H. Sun, S. Z. Qiao, J. Zou, G. Liu, S. C. Smith, H. M. Cheng, G. Q. Lu, Anatase TiO_2 single crystals with a large percentage of reactive facets. *Nature* **453**, 638–641 (2008).

25. L. Zhou, D. Smyth-Boyle, P. O'Brien, A facile synthesis of uniform NH_4TiOF_3 mesocrystals and their conversion to TiO_2 mesocrystals. *J. Am. Chem. Soc.* **130**, 1309–1320 (2008).

26. K. E. Lee, M. A. Gomez, S. Elouatik, G. P. Demopoulos, Further understanding of the adsorption mechanism of N719 sensitizer on anatase TiO_2 films for DSSC applications using vibrational spectroscopy and confocal Raman imaging. *Langmuir* **26**, 9575–9583 (2010).

Liu *et al. Sci. Adv.* 2015;1:e1500166   8 May 2015

7 of 8

27. W.-Q. Wu, Y.-F. Xu, H.-S. Rao, C.-Y. Su, D.-B. Kuang, Multistack integration of three-dimensional hyperbranched anatase titania architectures for high-efficiency dye-sensitized solar cells. *J. Am. Chem. Soc.* **136**, 6437–6445 (2014).

28. H. Wang, P. G. Nicholson, L. Peter, S. M. Zakeeruddin, M. Grätzel, Transport and interfacial transfer of electrons in dye-sensitized solar cells utilizing a Co(dbbip)$_2$ redox shuttle. *J. Phys. Chem. C* **114**, 14300–14306 (2010).

29. Y.-w. Jun, M. F. Casula, J.-H. Sim, S. Y. Kim, J. Cheon, A. P. Alivisatos, Surfactant-assisted elimination of a high energy facet as a means of controlling the shapes of TiO$_2$ nanocrystals. *J. Am. Chem. Soc.* **125**, 15981–15985 (2003).

30. A. S. Barnard, L. A. Curtiss, Prediction of TiO$_2$ nanoparticle phase and shape transitions controlled by surface chemistry. *Nano Lett.* **5**, 1261–1266 (2005).